Spatial and network principles behind neural generation of locomotion

Salif Komi[1], August Winther[1], Grace A. Houser[1], Roar Jakob Sørensen [1], Silas Dalum Larsen[1], Madelaine C. Adamssom Bonfils[1], Guanghui Li[1], Rune W. Berg[1*]

[1] Department of Neuroscience, Faculty of Health and Medical Sciences, University of Copenhagen
Blegdamsvej 3, 2200 Copenhagen, Denmark
*Correspondence (E-mail): runeb@sund.ku.dk (RWB)

ABSTRACT

Generation of locomotion is a fundamental function of the spinal cord, yet the underlying principles remain unclear. In particular, the relationship between neuronal cell types, networks and function has been difficult to establish[1,2]. Here, we propose principles by which functions arise primarily from spatial features of the cord. First, we suggest that distinct cell types with dissimilar length of projection constitute an asymmetrical "Mexican hat" topology, i.e. local excitation and surrounding inhibition, along the rostro-caudal axis. Second, the transversal segregation of cell types conveniently allows synapses to form with appropriate targets. We demonstrate these principles in a model of the mouse spinal cord, where networks are constructed by probabilistic sampling of synaptic connections from cell-specific projection patterns, which are gleaned from literature[3,4]. The cell-type distributions are derived from single-cell RNA sequencing combined with spatial transcriptomics[5]. We find that essential aspects of locomotion are recapitulated and easily controlled, and several experimental observations can now be explained mechanistically. Further, two main features are predicted: propagating bumps of neural activity and asymmetric neuronal projections with local excitation and wider inhibition. Besides linking cell types, structure and function, our approach provides a unifying framework for understanding motor activity across limbed and undulatory species.

Main

Rhythmic movements, such as walking or swimming, are generated by motor networks in the spinal cord known as central pattern generators (CPGs). These CPGs consist of a diversity of neurons with different genetic profiles. For many years, genetic tools have been used to classify neuronal cell types[2,4,6,7], operating under the assumption of a direct link between genetic identity and role in motor function[1]. While some genetically defined neurons have been associated with basic functions like rhythm generation in certain species[8,9], or with left-right and flexor-extensor alternation[10,11], individual cell types rarely appear to have a singular, well-defined role[1,7,12–14]. These perplexing results arise because the basic premise overlooks the influence of genetics on connectivity and how connectivity constrains electrical activity – and the connectivity is largely unknown. Although some connections to motoneurons, including reflex archs, have been mapped[15], these findings represent fragments of the surrounding circuit rather than the CPG network itself. Without an integrated understanding of how genetics, connectivity and dynamics relate to function, any theoretical framework will remain incomplete and insufficient to fully grasp motor behaviours. Here, we propose a solution to these open questions through principles that bind cell types to spatial features and link spatial network structure to functional dynamics.

Space as a principle

In many species, a clear feature of genetically identified cell types is their exquisite spatial organization[1,4,7]. They show transversal segregation and various patterns of projection in the rostrocaudal (RC), mediolateral (ML) and dorsoventral (DV) directions. For instance, in mice, a subset of V2a excitatory neurons upregulating the Vsx2 transcription factor, are located in intermediate laminae along the DV axis from where they exhibit strong projection biases in ventral and caudal directions (**Fig. 1A-C**). Another cell type, the V1 inhibitory interneuron, is known to localize ventrolaterally and to project primarily rostrally[17]. Altogether, the diversity of cell types forms a projection pattern with excitatory and inhibitory neurons that cover both longitudinal and transversal directions at different extensions (**Supp. Fig. 1**)[18,19].

A second key characteristic of central pattern generators (CPGs) is their ability to produce rhythmic activity. While pacemaker neurons have been suggested as a potential mechanism[12–14], there is limited evidence supporting their necessity, suggesting that rhythmicity may instead arise from network-level interactions[20]. Population recordings from the spinal cord during rhythmic activity demonstrate that all phases of the cycle are represented nearly equally within the neuronal population,

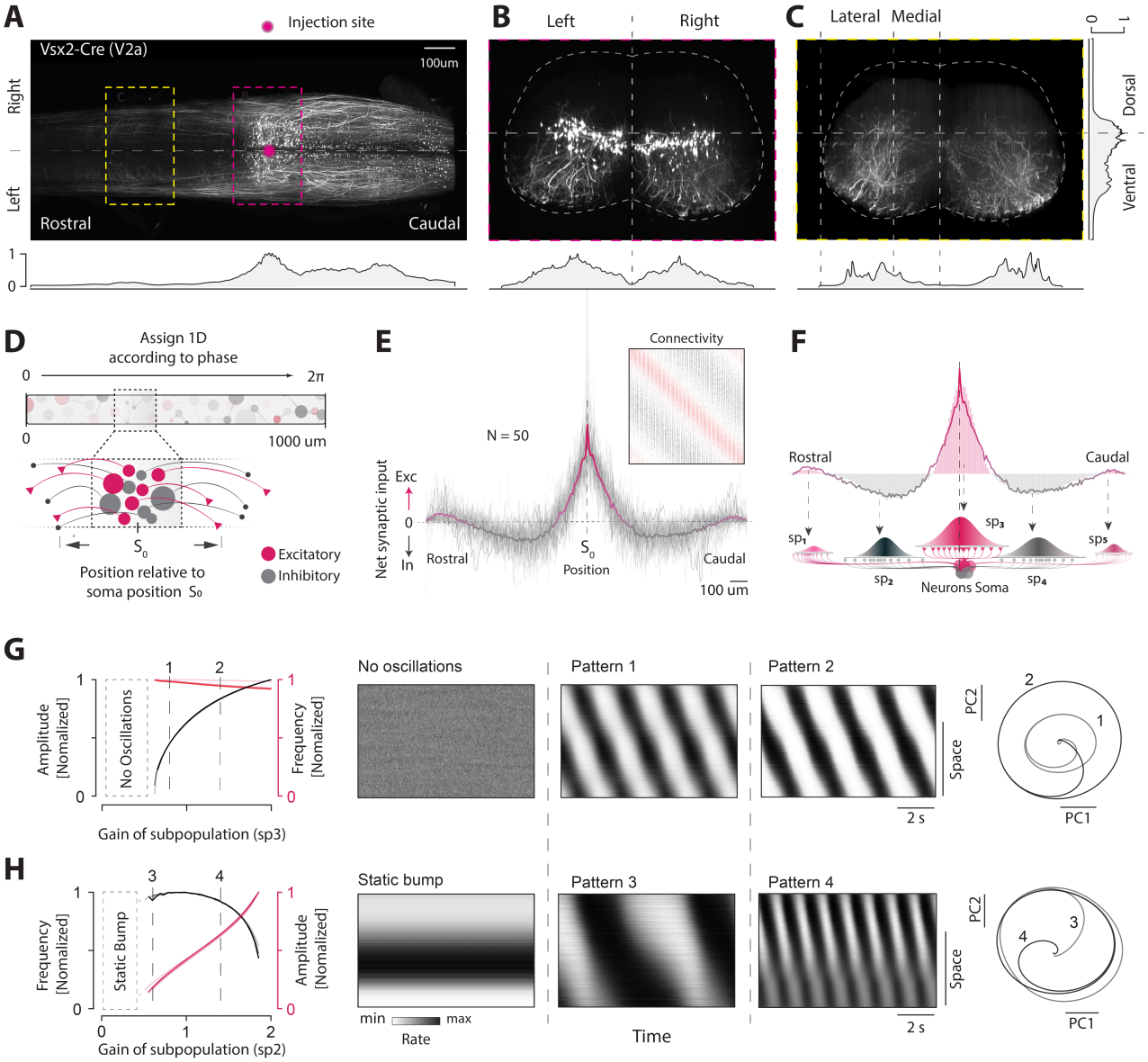

Fig. 1. | Space as a principle for rhythm generation with independent frequency and amplitude control. A, Ventro-caudal projection bias of a subset of the V2a excitatory neurons (Vsx2) revealed by a fluorescent reporter (AAV point injection, magenta) in the mouse lumbar spinal cord (dorsal view). **B**, Transverse section from A (magenta) shows somata and their axonal projections in ventral directions. **C**, Few axons also go in rostral direction (yellow highlight in A). **D**, Axonal projections from a given location, S_0, of excitation and inhibition (red/grey) of the model can be extracted by unfolding networks along the spinal axis[16]. **E**, This projectome and connectivity matrix (inset) reveals an asymmetric "Mexican hat" structure. **F**, Assigning cell types with projection bias (as in A) to individual lobes with Gaussian distributions of projections together comprise the net profile. **G-H**, The network generates rhythms with almost independent amplitude (G) and frequency (H) control using gain modulation of sub-populations (left). Patterns of firing rate activity (middle) for three values of gain (indicated, left). When increasing gain of local excitation (sp3), the frequency is almost constant (top, G) whereas the amplitude changes, visible as larger radius in the rotational dynamics (PC1-2, right). When increasing gain of rostral inhibition (sp2) the frequency changes without affecting amplitude, i.e. similar radius of rotation in PC-space (H, middle and right). Contrasts in A-C are individually enhanced. Data in A-C adapted from[5]

a phenomenon known as rotational dynamics[16,21–23]. To date, only one theoretical model, the Balanced Sequence Generator (BSG)[16] (**Supp. Fig 1**), has successfully explained these dynamics. This raises an intriguing question: how do rhythms and rotational dynamics emerge from such simple networks without the need for specialized pacemaker populations? The solution may lie in the theory of neural fields, which emphasizes the role of spatial organization in generating these patterns[24–26].

We thus ask whether spatial organization alone could constitute the foundation for motor functions. Here, we demonstrate this relationship by unfolding networks, that have rhythmogenic and rotational qualities[16], in space. We do so by ordering neurons according to their phase in the sequential activity and placing them on a line to mimick the spinal cord longitudinal axis (**Fig. 1D**). The assumption is that interneurons with similar phases have spatial proximity to minimize wiring cost (**Supp. Fig 2**). Excitatory (E) and inhibitory (I) neurons, located at S_0, make synapses on various targets along the line. When inspecting the net synaptic output from S_0 , i.e the sum of synaptic strengths, along the line, a striking picture emerges: Local excitation and long-range inhibition, which form an asymmetric profile resembling a “Mexican Hat” (**Fig. 1E**, **Supp. Fig. 2**). The profile has the same shape regardless of choice of S_0, albeit restricted by the boundaries of the cord. This is also apparent from the network connectivity matrix, where local excitation and longer range inhibition are visible as diagonal bands (inset, **Fig. 1E**).

We define the "projectome" as the net synaptic strength along the longitudinal axis of fibers arising from a single site. This structure that often adopts a "Mexican hat"-like topology due to the varying lengths of excitatory and inhibitory projections[24,25]. This projectome can emerge from combining multiple neuronal sub-populations with distinct projection patterns (**Fig. 1F**), as observed in spinal cord cell types (**Fig. 1A**). To investigate whether mapping of cell types to projectome features confers functional advantages, we constructed linear networks consisting of five sub-populations (sp1-5), each reflecting distinct aspects of the projectome. Synaptic probabilities for each cell type were modeled as Gaussian functions based on their mean projection length (d_p), width (θ_p), and gain (G_p), allowing different sub-populations to form synapses at varying distances. These terminals collectively form the projectome as five Gaussian lobes (sp1-5, **Fig. 1F**).

Networks of varying sizes were generated and simulated using a rate model formalism (see Methods). Remarkably, all networks produced rhythmic activity in response to constant input, regardless of their size. We then explored the impact of gain modulation of specific cell types and found that individual populations modulated distinct rhythmic properties. For instance, the amplitude could be selectively increased with minimal effect on frequency by enhancing local excitation in the central lobe (sp3, **Fig. 1G**). Conversely, modulating the gain of ascending inhibitory projections (sp2) allowed control of the frequency without altering amplitude (**Fig. 1H**). Interestingly, rhythmic activity could be slowed or halted while preserving static, localized neural activity. Similar effects were observed with modulation of other subpopulations (**Suppl. Fig. 2**).

These phenomena can be explained by the skewness of the projectome. Symmetric network topologies, characterized by localized excitation and global inhibition, are known to support stable "bumps" of activity[26], analogous to ring attractor dynamics in Drosophila[27]. However, when skewness is introduced into the projection profile, these activity bumps can transform into traveling sequences[25,26,28,29]. Thus, key functional dynamics — such as rhythms, rotations, traveling waves, and slow-downs/halts — emerge from, and are modulated by, a set of cell types with asymmetric projections. This principle forms the foundation of our findings.

Constructing the mouse spinal cord

Arranging cell types along a linear axis, as demonstrated above, can produce wave dynamics similar to those observed in undulatory species[32]. However, it has been widely assumed that limbed locomotion is fundamentally distinct due to the presence of multiple ipsilateral flexor-extensor pairs in the cervical and lumbar enlargements. This distinction, however, has not been rigorously tested, primarily due to experimental limitations. Given that a significant portion of vertebrate cell types have been conserved throughout evolution[1,15], we propose that the same spatial logic applies more broadly, enabling us to model limbed locomotion using the same framework. Accordingly, we extend and adapt our model to the mouse spinal cord.

First, we map the location of cell types using a combination of single-nucleus RNA-sequencing and spatial transcriptomics of a transverse section of the mouse lumbar spinal cord, previously obtained[5] (**Fig. 2A, Supp. Fig 3**). According to a harmonized cell type atlas[31], we resolve the locations of 69 (28 I, 38 E, 3 motoneurons) neuronal populations spanning the entire DV axis. This provides a quantitative measure of cell type distribution in a transverse section of the lumbar cord. The distributions resemble those established through other methods, e.g. Allen Mouse Spinal Cord Atlas (**Fig 2B, Supp. Fig 3**). We make the simplifying assumption that these distributions are preserved in longitudinal direction and extend the map (**Fig. 2C**). The purpose is to allow the projections of a given presynaptic neuron to target regions in both longitudinal and transverse directions. We aggregate populations of the same developmental origins[31] and consider these groups as our spinal cell types (**Supp. Fig. 3**). Since CPGs can function even after deafferentation[15], we focus on cells in the ventral territory of the spinal cord and do not include dorsal horn interneurons or sensory feedback. Besides motoneurons (Mn), we include eight cell types, the excitatory $V0v$, $V2a_{Vsx2+}$,$V2a_{Vsx2-}$ and $V3$, and inhibitory $dI6$, $V0d$,$V1$ and $V2b$ (color coded, **Fig. 2D**).

Second, we assign a spatial probability of projection, which is adjusted for each cell type in accord with empirical observations[3,4] (**Fig. 2D**, **Supp. data table 1**). For instance, V2a have both local and longer range ipsilateral projections, the

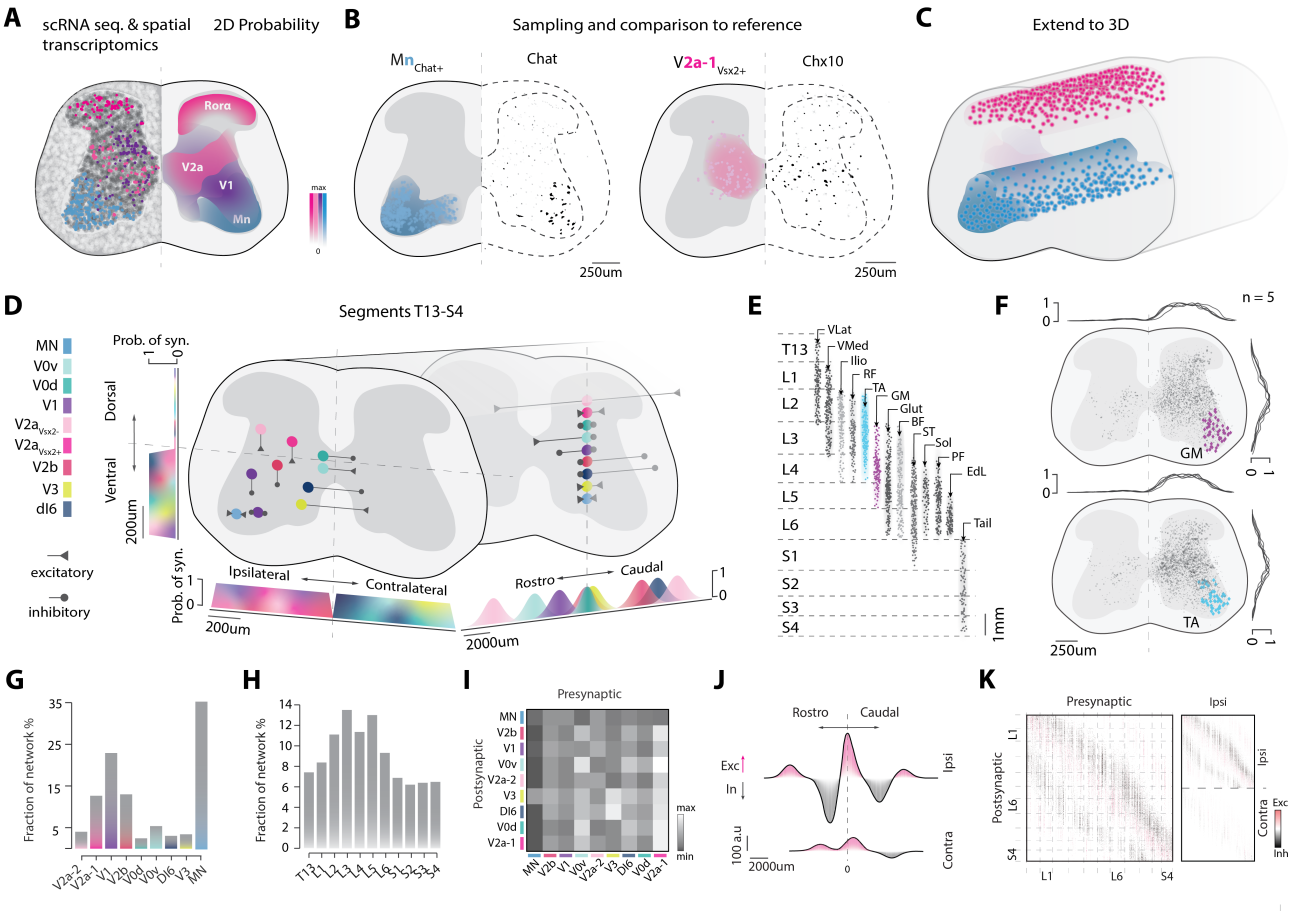

Fig. 2. | **Motor function associated with spinal cell types through spatial segregation. A**, Cell types distributions are identified using scRNA sequencing and mapped in transverse plane by spatial transcriptomics. **B,** Comparison of two types, Mn (blue) and $V2a_{Vsx2+}$ (magenta), sampled from A, with the empirical maps of their molecular markers, ChAT and Chx10/Vsx2, respectively[30]. **C,** The distributions are extended longitudinally to model the lumbar spinal cord volume. **D**, Nine cells types are included in a model of the lumbo-sacral region of the cord (segments T13-S4). Cell type specific projection patterns are modelled as independent Gaussians along the RC, ML, and DV axes. Each Gaussian defines a probability of forming a synapse with any target neuron falling in the distribution. **E,** Segmental hindlimb motoneurons pools distributions as assigned in the model. **F,** Locations of the premotor interneurons (black) from the flexor (Tibialis Anterior (TA)) and extensor (Medialis Gastrocnemius (MG)) motoneurons (colors), including their inferred distributions (black lines). **G**, Cell type fractions within the population used in the model. **H**, Distribution of neurons across spinal segments. **I**, Cell type connectivity matrix (rectified and normalized). **J**, Network projectome decomposed in its ipsilateral and contralateral components. **K**, Pairwise connectivity matrix, **W**. Data in A[5,31] and E[30] reanalyzed with permission.

V0, dI6 and V3 are primarily commissurally projecting and V1 and V2b have mainly ascending and descending directions, respectively. Differential expression analysis of marker genes of long range and local projections[2] corroborate these choices (**Supp. Fig. 3**). We include segments T13 to S4 and distribute hindlimb motoneuron pools according to their identity and known segmental locations[33] (**Fig. 2E**). Sample premotor interneurons are spatially intermingled in agreement with established experimental tracings[34] (**Fig. 2F**). The relative fraction of cell types used in the model (**Fig. 2G**) is similar to cell counts reported for the mouse[5,31]. The lumbar enlargement also has a larger fraction of cells in general (L2-L5, **Fig. 2H**). These assumptions allow predicting the connection probability between cell types (**Fig. 2I**, **Suppl. Fig. 7**), the ipsi- and contralateral projectome (**Fig. 2J**) as well as the actual connectivity matrix (**Fig. 2K**). Now we have constructed a model network of the lumbar spinal cord, that serves both as validation of the approach against experimental observations and as a prediction of future experiments. Most importantly, we can test if useful spatio-temporal activity can emerge out of this network model.

Emergent spatial dynamics

As introduced previously, we employ a rate-based formalism to investigate the dynamics of our models[16] (**Fig. 1**). In this framework, the firing rate of each neuron is a smooth function where the slope is the gain (**Fig. 3A**). The gain and input can be modulated by e.g. descending fibers. We ask whether descending excitation and modulation recapitulate locomotion dynamics, as observed experimentally. We introduce two descending inputs: one glutamatergic from the caudal medulla (LPGi[35]) that excites cells in the intermediate laminae, and raphe fibers releasing serotonin, which causes gain modulation in cells expressing 5-HT receptors 7 (upregulation) and 1b (downregulation) (**Fig. 3B**, **Suppl. Video 1**).

We want to predict the emergent dynamics of our network under these modulations. Conveniently, the rate-based formalism results in a set of coupled dynamical equations, where $\mathbf{W}$, i.e the connectivity matrix, plays a important role in linking structure to function. The eigenspectrum—comprising all eigenvalues—provides essential insights into the network dynamics (**Fig. 3B**). Specifically, if the dominant mode, characterized by the largest real part, exceeds the stability threshold and possesses an imaginary component, the network is predicted to exhibit oscillatory behavior. The spectrum of our network reveals two prominent complex eigenvalues associated with rhythmic activities (**Fig. 3C**), termed mode 1 and mode 2. Mode 1 is associated with two propagating waves, each carrying two "bumps" of activity, alternating between the right and left hemicords, which we interpret as walking (**Fig. 3D, Suppl. Video 2**). In contrast, mode 2 corresponds to synchrony between these waves, representing a bounding mode. We consider two pairs of antagonistic motoneuron pools for comparison with experimental data[33] . These motoneurons are recruited by local premotor interneurons that carry the spatial "bumps" of activity. In our hands, the structure of the bumps approximately matches the extent and alternation of pools of antagonist muscles (right, **Fig. 3D, Supp. Fig. 8**).

We next simulate network behavior under constant LPGi activation while gradually increasing serotonin levels (**Fig. 3E**, top). Serotonin selectively affects populations expressing its receptors, modifying the projectome in a distinct manner (**Fig. 3E**, bottom). These adjustments lead to shifts in motor behavior. At low serotonin levels, the projectome displays minimal asymmetry, producing a slow, left-right alternating pattern that mimics walking. As 5-HT input increases, the projectome becomes increasingly asymmetric, giving rise to faster locomotor patterns such as trotting and bounding (**Fig. 3F-I**). This progression is also reflected in the shifting positions of the eigenvalues (**Fig. 3E**). Overall, the population exhibits all phases and shows rotational dynamics in PCA space (**Fig. 3K-L**).

In summary, our model of the mouse spinal cord, grounded in the principle of linking structure to function and cell types, successfully generates activity that aligns with realistic motor behaviors. The explicit incorporation of genetic cell types allows computational manipulation experiments in parallel with reported experimental findings.

Manipulation of cell types

The common approach in investigating spinal motor function has been to perturb cell types and interpret the effects on activity. One example is the V1 inhibitory interneurons, which were manipulated using various genetic approaches. The general observation is that silencing the V1 neurons causes a slowing of locomotor-like rhythmicity such that these interneurons provide a means to control frequency[36,37]. The observation that removing inhibition causes a slow-down is counter-intuitive and has been difficult to explain. Furthermore, perturbations of V1 neurons seem to have other effects than just frequency, like increase in spiking and flexor-extensor duty cycle[38]. Could these and other previous experiments, like silencing the V0 and blocking all inhibition, be explained in our framework?

Here, we first perform a "silencing" of the V1 interneurons in the model. This is done by selectively first hypopolarizing before completely ablating the V1 population (**Fig. 4A-C**). The result is a slow down of the rhythm, in agreement with past results. Also, the burst amplitude increases, whereas the left/right and flexor/extensor phase relations are unaffected (purple **Fig. 4B-C**). Although this accord is reassuring, it does not itself explain the mechanism. We suggest the following explanation, which is extracted from the spatial principle (**Fig. 1H**). In the intact situation, the ascending inhibition (sp_2, **Fig. 1F**) prevents the spread of local excitation in the rostral direction. This effect combined with an excitatory projection-bias towards the tail

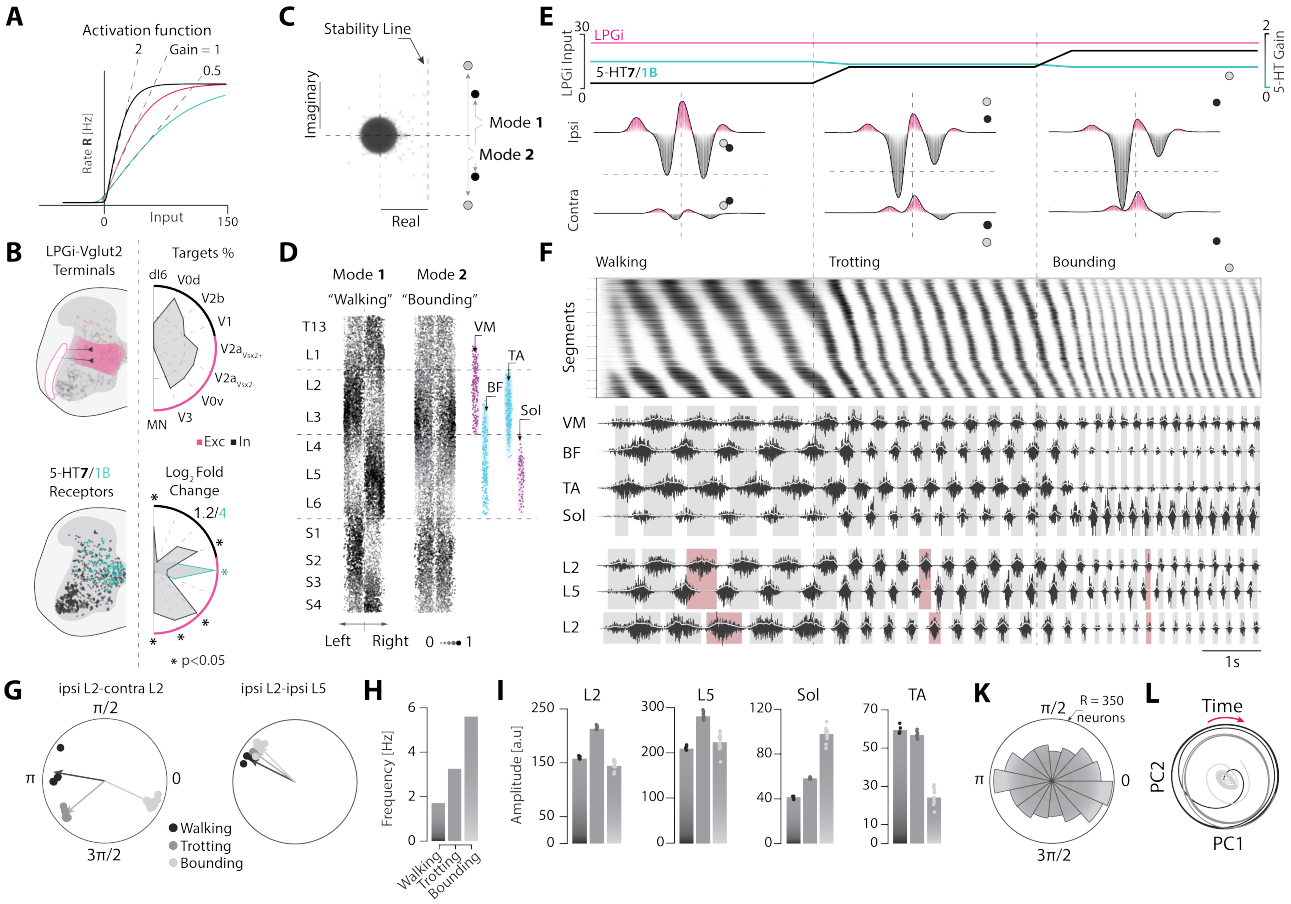

Fig. 3. | **Mouse locomotion: Emergent spatio-temporal dynamics of the model. A**, The activation function (hyperbolic tangent, see Methods) of the neurons in the model. **B**, Top: Location of the terminals of the LPGi fibers and targeted cell types. Bottom: Location of cells differentially expressing 5-HT7 (black) or 5-HT1B (cyan) receptors and relative expression level (log2 fold change) of both receptors in cell types. Radius values are indicated for both receptors. Stars indicate a significant change in expression. **C**, The eigenspectrum of W has two dominant eigenvalues, representing two modes, above stability line and with imaginary parts, hence oscillatory. **D**, The corresponding firing activity (illustrated as size of dots) of neurons in space of the two modes, which represents either right-left alternation (Walking) or synchrony (Bounding). Selected flexor (blue) and extensor (magenta) motoneuron pools are indicated.**E**, Top: the descending input (constant glutamatergic drive from LPGi, pink) and the gain of the cells expressing 5HT7 (increasing , black) and 5HT1B (decreasing, cyan) receptors. Bottom: the corresponding projectome adjusted for the modulated gain, and the dominant eigenvalues indicated (gray and black dots). The eigenvalues change place as the gain is increased and the gait is similarly changed from walking, trotting to bounding. **F**, Mode 1 (walking) has "bumps" of activity propagating across segments in caudal direction (Left hemicord). Middle: increase in frequency (Trotting), with same sequential muscular activity. Right: Highest frequency, with a switch in gait from the change between mode 1 and 2. The phase right/left L2 are now in phase. (bottom). **G**, Polar respresentation of right/left L2 phase and L2-L5 phase. **H**, bar graph of locomotor frequency during walking, trotting and bounding. **I**, corresponding muscle amplitudes of those behaviors. **K**, Phase distribution of all neurons, indicates rotational dynamics. **L**, population dynamics projected onto the first two PC, based on the walking activity. The trotting and bounding are in a subspace (reduced variance, gray lines).

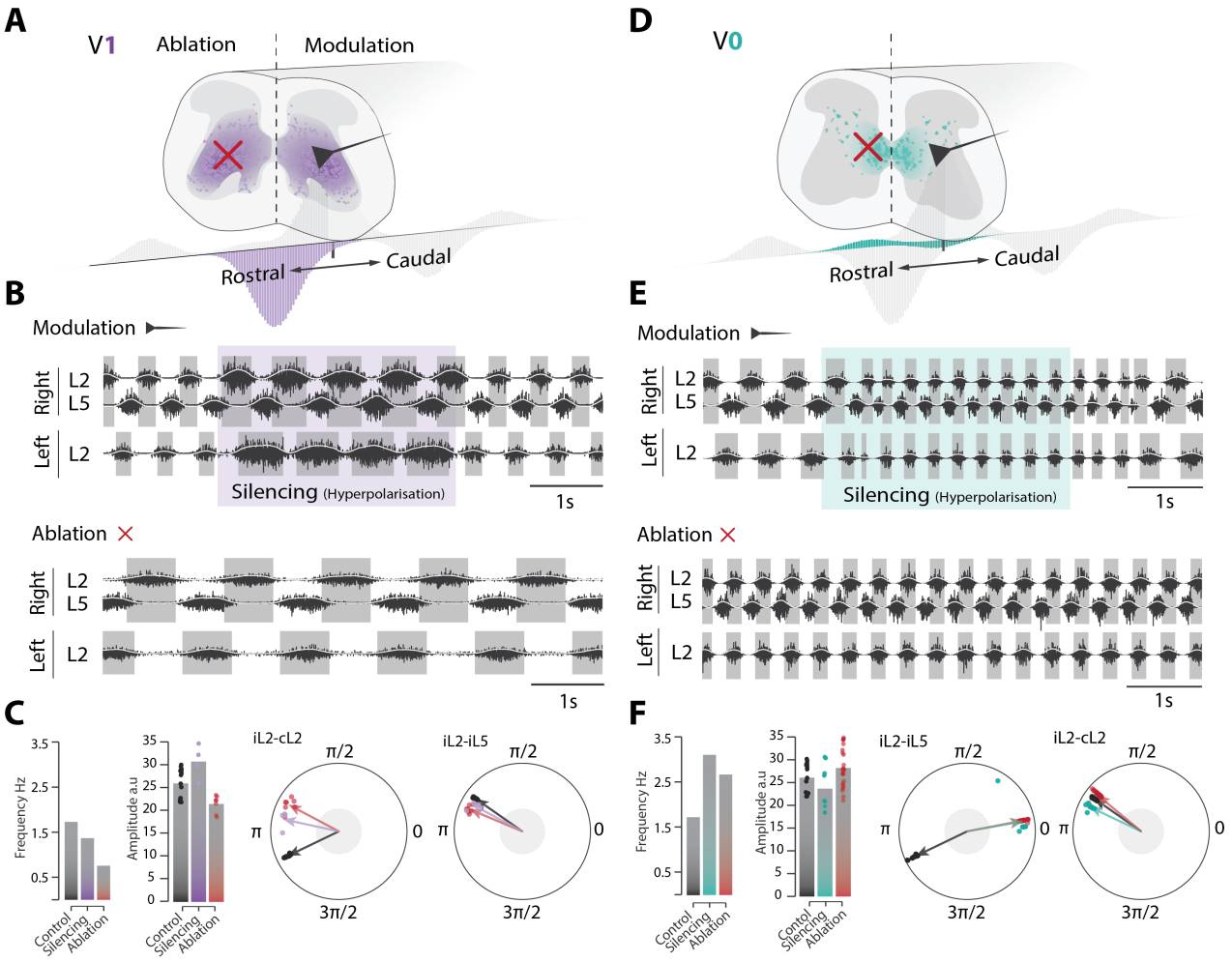

Fig. 4. | **Manipulation of V1 and V0 cells in model. A**, V1 cell type is manipulated either by hyperpolarization, imitated by a black synapse, or simply removed from the network (ablated, red cross). Only the rostral lobe of the projectome is affected (purple distribution, bottom). **B**, Slowing of motor nerve activity of spinal segments L2 and L5 as a concequence of V1-silencing (top, purple area), and after V1-ablation bottom. **C**, Mean frequency decreases with silencing and ablation, while the amplitude is increase (silencing) or decreased (ablation, bar graphs, left). Phase relations of right/left (L2) and ipsilateral (L2-L5) are large unaffected (polar plots, black: control, purple: silencing, red: ablation). **D**, V0 manipulation by silencing or ablation. Contralateral contributions to the spinal pojectome is now affected (cyan, bottom). **E**, Motor nerve activity before and during V0-silencing has two consequences; a speed up and a right/left phase shift (cyan area, top). Ablation has similar effects (bottom). **F**, Mean frequency increases during V0 silencing (cyan) and ablation (red) compared with control (black). The amplitudes are largely unaffected (right bar graphs). The right/left phase of L2 switch from alternation to synchrony (cf. black, cyan and red, left polar plot) while the phase of ipsilateral L2-L5 remains unaffected (right polar plot).

causes the bump of activity to propagate caudally. When decreasing or eliminating the ascending inhibition (V1 subpopulation) the bump of local excitation will remain for longer time, which effectively increases the descending inhibition and therefore cause a slow-down of the caudal propagation. The reverse is also true: when ascending inhibition is strengthened, the bump will move faster in the caudal direction (**Fig. 1H**). Descending ipsilateral inhibition is provided by the V2b cells[39], which are less numerous than the V1 cells[11], and their respective ratio ensures an asymmetry in longitudinal inhibition. Also, the amplitude of the motor output is generally increased due to unbalancing of the E/I ratio when silencing either V1 or V2b. Silencing both V1 and V2b will result in a fast uncontrolled spread of excitation, resulting in a collapse of flexor/extensor alternation[11]. A similar effect is seen during pharmacological blocking of inhibition albeit with stronger and long-lasting effects (**Suppl. Figure 8**).

Another experimental manipulation has targeted the V0 interneurons. Genetic ablation of V0 is known to cause quadrupedal hopping at all frequencies of locomotion[40]. We test the effect of V0 manipulation in our model by first hyperpolarizing the V0, which causes a reduction in the commissural projectome[19] (cyan **Fig. 4D**). The hyperpolarization causes both an increase in locomotor frequency and a right-left L2 synchronization, i.e. a hopping (cyan area, top **Fig. 4E**). Complete ablation of V0 cells has similar effects (bottom). The ipsilateral L2-L5 phase and the muscle amplitudes are largely unaffected, while the right-left coordination changes (**Fig. 4F**).

In conclusion, we demonstrate that previous experimental observations can be reproduced and explained by mechanistic principles (**Suppl. Fig. 2**): Function arise out of dynamics, dynamics arise out of the network and the network is build out of cells types with spatial segregation and projection biases.

Discussion

Although cell types are often assumed to be linked to spinal motor function[1,4,41], an understanding of how they are linked has been absent from the literature. An important clue is that many molecular markers are associated with either axon guidance, cell adhesion or general spatial organization[31]. Here, we propose that motor functions emerge out of spatial structure, where the location of cell types together with their longitudinal projections constitute the principle of organization. Asymmetric projection with local excitation and long-range inhibition is essential for rhythm generation and sequential activation of motoneurons. The link between cell type and function is established via dynamics in the network, which is shaped by a combination of the projectome and spatial location.

We test our approach in models, where the spatial distribution of cell types is extracted empirically using single cell sequencing combined with spatial transcriptomics and where the cell type projectome composition is gleaned from the literature (**Fig. 2**). We find that dissimilar projection lengths readily give rise to an asymmetric "Mexican hat" organization, i.e. local excitation and long range inhibition. The asymmetry causes an emergent bump of local activity to propagate in the caudal direction (**Fig. 3**). Since the shape and size of the projectome determines properties of the activity, e.g. frequency and amplitude (**Fig. 1**), modulation of individual cell types that make up the projectome constitutes a convenient means of descending control. Hence, modulation of cell types with well-characterized effects, e.g. the V0 and V1, resulted in behaviors in accordance with experimental reports (**Fig. 4, Supp. Fig. 4-6**). Notably, our model is capable of generating appropriate behavior without requiring fine adjustment of particular synaptic connectivity weights or cellular mechanisms like pacemaker cells.

This approach stands in contrast to conventional CPG models where the network is constrained by posited rules, e.g. modules with reciprocal inhibition, feed-forward excitation, and where rhythms are generated by cellular pacemaker properties[15,41]. Such modular organization, inspired by the half-center network[42] , has difficulties explaining gradual slowdown and stopping of movement. This is due to both the autonomous nature of rhythmogenic cells and the abrupt transition of activity between antagonistic modules with recurrent unbalanced excitation[43]. When agonist modules are active the antagonistic modules are kept silent by reciprocal inhibition and vice versa. Hence, all cells have either same or opposite phase, and this is in disagreement with the continuous progression of cyclic activity, i.e. rotational population dynamics, observed throughout the neuronal population[16,21–23]. Instead, we propose a spatial organization where adjustment of excitatory and inhibitory lobes of the projectome allows full control of all aspects of rhythmic activity including slow down and stop at any phase of the cycle (**Fig. 1**, **Suppl. Fig. 2**).

Our approach predicts traveling waves in the spinal cord during locomotion even in tetrapods. This idea is not new and has been proposed and demonstrated in various species[17,44–47]. Propagation of waves in limbed vertebrates has also been demonstrated, e.g. in frog[48], terrestrial stepping of salamander[49], and newborn rodents[50,51], which could also explain a wave within motoneuron pools[51–53]. Systemic block of inhibition leads to a seizure-like fast wavefront that effectively synchronizes nerve activity[54] (**Supp. fig. 7**). Surface field potentials show sinusoidal waves in cats under fictive rhythmic scratching[55,56]. Nevertheless, another report was unable to substantiate such a wave among interneuron spiking activtiy[57], which suggests the issue could be more complicated and even cell type specific if it is a propagating wave. This issue remains to be investigated further in future studies.

Methods

Spinal Injections, Tissue Clearing, and Imaging

The data and methods related to figure 1A-C, are provided and reanalysed with permission from a previous publication[5]. Images in Fig. 1A-C were subject to individual contrast enhancement.

Quantification of Projections

The 3D images were processed using an open access software (TRAILMAP)[58] with default parameters, and another open access analysis tool for light sheet microscopy files and which is optimized for the pretrained model 3 from DeepTrace, DeepTrace). This processing generated a 3D probability map of axons, which was projected onto the longitudinal axis to quantify local, rostral, and caudal projections.

Immunohistochemistry

All immunohistochemistry images were adapted from the Allen Brain Atlas of the Mouse Spinal Cord (Allen Brain Atlas)[30].We exported images from the expression mask, inverted their color, and converted them to gray scales. Some linear transformation (shearing, scaling) were applied to fit our layout.

Model framework

In all simulations presented in this report, we employed a rate model formalism governed by the following differential equation:

$$\tau_i \dot{x}_i(t) = -x_i(t) + \sum_{j=1}^{N} w_{ij} F(x_j(t)) + I_i(t) + \varepsilon_i(t)$$

where

$$F(x) = \begin{cases} T \cdot \tanh\left(\frac{x-T}{T}\right) + T, & \text{for } x \leq 0 \\ f_{\max} \cdot \tanh\left(\frac{x-T}{f_{\max}}\right) + T, & \text{for } x > 0 \end{cases}$$

Here, the subscripts denote the neuron index. The parameter τ (set to 50 ms) represents the integration time constant, $x_i(t)$ is the input potential of neuron i, and $\dot{x}_i(t)$ is its time derivative. w_{ij} is the synaptic weight of neuron j impinging on neuron i. $I_i(t)$ is the external input to neuron i, and $\varepsilon_i(t) \sim \mathcal{N}(0, 0.4\,\text{mV})$ is a Gaussian noise term with a mean of 0 mV and standard deviation of 0.4 mV. The function $F(x)$ is a compound tanh activation function that maps input potential to firing rate, with T as a threshold parameter and $f_{\max}$ as the maximum firing rate. This function ensures non-negative firing rates across all neurons. We numerically integrated this equation for each neuron in the network using the Euler method with a time step of $\Delta t = 1$ ms. The output of each simulation was a matrix representing the firing rate of every neuron over time.

Simulation Analysis

Principal component analysis was performed on the $T \times N$ rate matrix using MATLAB's `pca()` . Oscillatory frequency (oscillations/second, Hz) was estimated by computing the mean temporal distance between peaks in the firing rates projected onto the first principal component. Oscillatory amplitude was estimated as the mean root mean square (RMS) over firing rates of all units in a simulation,

$$amplitude = \frac{1}{N} \sum_{i=1}^{N} \sqrt{\frac{1}{T} \sum_{t=1}^{T} r_{i,t}^2}$$

with N denoting the size of the network, T the simulation duration and $r_{i,t}$ the mean-subtracted firing rate of neuron i at time t.

Random Networks

100 random networks of size N = 500 were generated. In all networks, excitatory (inhibitory) neurons constituted $1/2$ of the N units. A synapse from neuron j to neuron i was placed in an $N \times N$ matrix $\boldsymbol{W}$, where columns denote source neurons and rows denote target neurons, using a binomial draw over the synapse probability, $p_{\text{synapse}} = 0.1$. Synaptic weights w_{ij} were sampled from a Gaussian distribution $w_{ij} \sim \mathcal{N}(\mu = 1, \sigma = 0.1)$. In accordance with Dale's principle, inhibitory synapses were multiplied with -1 such that inhibitory- and excitatory columns in $\boldsymbol{W}$ were strictly nonpositive and nonnegative, respectively.

Detailed balance between excitation and inhibition[59–61] was imposed on $\boldsymbol{W}$ such that $\sum_{j=1}^{N} w_{ij} = 0$ for each row i. Finally, the diagonal of $\boldsymbol{W}$ was set to zero, removing self-synapses. Random oscillatory networks were assigned a 1D spatial coordinate based on a phase-space coherence rule. From the connectivity $\boldsymbol{W}$ and the coordinates, the synapse-weighted relative distances at which excitatory and inhibitory units tended to project was averaged over all (n=50) networks.

Spatial 1D Networks

Networks of varying sizes ($N = 200$, $N = 500$, $N = 1000$, $N = 2000$, $N = 5000$, and $N = 10000$) were structured based on projection profiles revealed by unfolding random, oscillatory networks. The N neurons in each network were divided into five subpopulations: sp1, sp2, sp3, sp4, and sp5. Each neuron was assigned a 1D spatial coordinate, uniformly distributed between 0 and the defined network length, L_N.

A Gaussian distribution, $\mathcal{N}(d_n, \theta_n)$, was fit to each bump in the unfolded projection profile and assigned to each subpopulation as the connection probability distribution over pairwise distances, $d \in [-L_N, L_N]$. Thus, the spatial connectivity structure of each network was parameterized as a mixture of five translationally invariant Gaussians:

$$P(d) = \sum_{n=1}^{5} G_n \mathcal{N}(d_n, \theta_n)$$

where G_n is a scaling parameter, d_n is the mean projection distance, and θ_n is the variance around the mean for subpopulation n. An $N \times N$ pairwise distance matrix D was instantiated such that d_{ij} represents the spatial distance between neurons i and j. This matrix was binarized using a binomial sampling process based on the spatial projection probabilities for the five subpopulations. The resulting binary connectivity matrix was element-wise multiplied by an $N \times N$ gain matrix, where synaptic weights were Gaussian-sampled, similar to the method used for random network generation. Finally, we enforced detailed balance to produce the final connectivity matrix, W.

Single cell RNA sequencing and Spatial Transcriptomics

Curated and annotated single-cell/nucleus RNA sequencing datasets were obtained from the Gene Expression Omnibus: GSE184370(single nucleus[5]), GSE184369 (spatial transcriptomics[5]), and the SeqSeek repository[31]. Our primary single-cell dataset was the labeled data from SeqSeek, which classifies neurons into 69 genetically distinct populations (28 inhibitory, 38 excitatory, and 3 motoneuron-related). We used the developmental lineage labels from[31] as a coarser grouping to define our cell types for further analysis.

Estimation of 2D Spatial cell type distributions

To determine the spatial distributions of the labeled cell types, we deconvolved the spatial transcriptomics data with the single-nucleus RNA sequencing data using robust cell type decomposition (RCTD)[62]. We applied default parameters, with the doublet mode disabled, yielding a matrix of 9755 2D spatial locations x 69 populations. This matrix assigns a weight to each population for each spatial location. After log-normalizing and scaling the matrix columns to a [0,1] range, we applied a cutoff at the mean weight to sharpen the spatial densities. The resulting distributions of each cell type closely aligned with their known locations as verified through other methods (e.g., immunostaining, in situ hybridization).

Mouse Network Construction and Connectivity

To construct the network, we first defined the spatial arrangement of the neurons. For each neuron population p, we used the 2D probability matrix $\mathbf{P}_p(x,y)$ derived from transcriptomics data to sample neuron locations. Specifically, we binomially sampled the 2D spatial density $\mathbf{P}_p(x,y)$ to obtain a binary matrix $\mathbf{M}_p(x,y)$ where:

$$\mathbf{M}_p(x,y) \sim \text{Binomial}(1, \mathbf{P}_p(x,y))$$

Here, a value of $\mathbf{M}_p(x,y) = 1$ indicates the presence of a neuron at coordinates (x,y). Each neuron was then assigned a z-coordinate by sampling from a uniform distribution over the range $[1, L]$, where L is the network's longitudinal length:

$$(x_i, y_i, z_i) = (x_i, y_i, \mathcal{U}(1, L))$$

For motoneurons, we adapted this approach by using a refined longitudinal distribution $P_z^{\text{moto}}(z)$ based on known motor column locations:

$$z_i \sim P_z^{\text{moto}}(z), \quad \text{for motoneurons}$$

Given a density parameter D, we repeated these operations D times in order to control the overall number of neurons in the network.

To determine synaptic connectivity, we computed the pairwise distances between neurons in each spatial dimension independently:

$$d_{X,ij} = x_i - x_j, \quad d_{Y,ij} = y_i - y_j, \quad d_{Z,ij} = z_i - z_j$$

We then modeled the probability of a synaptic connection between neurons i and j using Gaussian distributions for each dimension:

$$P_X^p(d_{X,ij}) \sim \mathcal{N}(\mu_X^p, \sigma_X^p), \quad P_Y^p(d_{Y,ij}) \sim \mathcal{N}(\mu_Y^p, \sigma_Y^p), \quad P_Z^p(d_{Z,ij}) \sim \mathcal{N}(\mu_Z^p, \sigma_Z^p)$$

where μ_X^p, μ_Y^p, and μ_Z^p are the means, and σ_X^p, σ_Y^p, and σ_Z^p are the standard deviations estimated from axonal projection data. The overall synaptic probability was computed as:

$$\mathbf{P}_{syn}(i,j) = \left(P_X^p(d_{X,ij}) \cdot P_Y^p(d_{Y,ij}) \cdot P_Z^p(d_{Z,ij})\right)^{1/3}$$

This combines the probabilities from each dimension into a single measure of connection likelihood. We then binarized this probability to create a binary adjacency matrix $\mathbf{A}$:

$$\mathbf{A}(i,j) \sim \text{Binomial}(1, \mathbf{P}_{syn}(i,j))$$

where $\mathbf{A}(i,j) = 1$ indicates a synaptic connection between neurons i and j. To finalize the connectivity matrix, each neuron population p was assigned a gain parameter g_p. The final connectivity matrix $\mathbf{W}$ was obtained by scaling the binary adjacency matrix $\mathbf{A}$ with these gains:

$$\mathbf{W}(i,j) = g_p \cdot \mathbf{A}(i,j), \quad \text{for neurons } i \text{ in population } p$$

This approach ensures that each neuron's connectivity is appropriately scaled according to its population-specific gain.

Acknowledgements

This work was supported by The Lundbeck Foundation (no. R366-2021-233, R.W.B.), Novonordisk foundation (no. NNF23OC0082192, R.W.B), and The Swiss National Science Foundation (no. SNF Postdoc.Mobility P500PB_206824, S.K.). We would like to thank Prof. Grégoire Courtine for generously sharing the Vsx2 tracing data. We extend our gratitude to Prof. Claudia Kathe for her help and technical expertise.

Author contributions

R.W.B., S.K. A.W. conceived the original idea. G.H., G.L., and M.C.A.B. collected the data and analyzed some of the data. S.K. and A.W. performed the model simulations. S.K. A.W. and R.W.B. designed, and developed the theory. G.H., R.J.S., S.D.L., M.C.A.B., G.L., S.K., R.W.B., analyzed the experimental data. S.K., R.W.B. wrote the manuscript.

Competing interests

The authors declare no competing interests.

References

1. Sengupta, M. & Bagnall, M. W. Spinal Interneurons: Diversity and Connectivity in Motor Control. *Annu. Rev. Neurosci.* **46**, 79–99, DOI: 10.1146/annurev-neuro-083122-025325 (2023).
2. Osseward, P. J. *et al.* Conserved genetic signatures parcellate cardinal spinal neuron classes into local and projection subsets. *Science* **372**, 385–393, DOI: 10.1126/science.abe0690 (2021).
3. Alaynick, W. A., Jessell, T. M. & Pfaff, S. L. SnapShot: Spinal Cord Development. *Cell* **146**, 178–178, DOI: 10.1016/j.cell.2011.06.038 (2011).
4. Goulding, M. Circuits controlling vertebrate locomotion: moving in a new direction. *Nat Rev Neurosci* **10**, 507–518, DOI: 10.1038/nrn2608 (2009).
5. Kathe, C. *et al.* The neurons that restore walking after paralysis. *Nature* **611**, 540–547, DOI: 10.1038/s41586-022-05385-7 (2022).
6. Levine, A. J. *et al.* Identification of a cellular node for motor control pathways. *Nat. Neurosci.* **17**, 586–593, DOI: 10.1038/nn.3675 (2014).
7. Bikoff, J. B. *et al.* Spinal Inhibitory Interneuron Diversity Delineates Variant Motor Microcircuits. *Cell* **165**, 207–219, DOI: 10.1016/j.cell.2016.01.027 (2016).
8. Song, J. *et al.* Multiple Rhythm-Generating Circuits Act in Tandem with Pacemaker Properties to Control the Start and Speed of Locomotion. *Neuron* **105**, 1048–1061, DOI: 10.1016/j.neuron.2019.12.030 (2020).
9. Brocard, F. *et al.* Activity-Dependent Changes in Extracellular Ca2+ and K+ Reveal Pacemakers in the Spinal Locomotor-Related Network. *Neuron* **77**, 1047–1054, DOI: 10.1016/j.neuron.2013.01.026 (2013).
10. Zhang, Y. *et al.* V3 Spinal Neurons Establish a Robust and Balanced Locomotor Rhythm during Walking. *Neuron* **60**, 84–96, DOI: 10.1016/j.neuron.2008.09.027 (2008).
11. Zhang, J. *et al.* V1 and V2b interneurons secure the alternating flexor-extensor motor activity mice require for limbed locomotion. *Neuron* **82**, 138–150, DOI: 10.1016/j.neuron.2014.02.013 (2014).
12. Koronfel, L. M., Kanning, K. C., Alcos, A., Henderson, C. E. & Brownstone, R. M. Elimination of glutamatergic transmission from Hb9 interneurons does not impact treadmill locomotion. *Sci. Reports* **11**, 16008, DOI: 10.1038/s41598-021-95143-y (2021).
13. Dougherty, K. J. & Ha, N. T. The rhythm section: an update on spinal interneurons setting the beat for mammalian locomotion. *Curr. Opin. Physiol.* **8**, 84–93, DOI: 10.1016/j.cophys.2019.01.004 (2019).
14. Rancic, V. & Gosgnach, S. Recent insights into the rhythmogenic core of the locomotor cpg. *Int. J. Mol. Sci.* **22**, 1–11, DOI: 10.3390/ijms22031394 (2021).
15. Grillner, S. & El Manira, A. Current principles of motor control, with special reference to vertebrate locomotion. *Physiol. Rev.* **100**, 271–320, DOI: 10.1152/physrev.00015.2019 (2020).
16. Lindén, H., Petersen, P. C., Vestergaard, M. & Berg, R. W. Movement is governed by rotational neural dynamics in spinal motor networks. *Nature* **610**, 526–531, DOI: 10.1038/s41586-022-05293-w (2022).
17. Sengupta, M., Daliparthi, V., Roussel, Y., Bui, T. V. & Bagnall, M. W. Spinal V1 neurons inhibit motor targets locally and sensory targets distally. *Curr. Biol.* **31**, 3820–3833, DOI: 10.1016/j.cub.2021.06.053 (2021).
18. Bannatyne, B. A. *et al.* Excitatory and inhibitory intermediate zone interneurons in pathways from feline group I and II afferents: differences in axonal projections and input. *The J. Physiol.* **587**, 379–399, DOI: 10.1113/jphysiol.2008.159129 (2009).
19. Moran-Rivard, L. *et al.* Evx1 Is a Postmitotic Determinant of V0 Interneuron Identity in the Spinal Cord. *Neuron* **29**, 385–399, DOI: 10.1016/S0896-6273(01)00213-6 (2001).
20. Harris-Warrick, R. M. & Ramirez, J.-M. Neural Networks for the Generation of Rhythmic Motor Behaviors. In *Neurobiology of Motor Control*, 225–262, DOI: 10.1002/9781118873397.ch8 (2017).
21. Bush, N. E. & Ramirez, J.-M. Latent neural population dynamics underlying breathing, opioid-induced respiratory depression and gasping. *Nat. Neurosci.* **27**, 259–271, DOI: 10.1038/s41593-023-01520-3 (2024).
22. Wimalasena, L. N., Pandarinath, C. & Au Yong, N. Spinal interneuron population dynamics underlying flexible pattern generation. *BioRxiv* (2024).

23. Churchland, M. M. *et al.* Neural population dynamics during reaching. *Nature* **487**, 51–56, DOI: 10.1038/nature11129 (2012).

24. Amari, S.-i. Dynamics of pattern formation in lateral-inhibition type neural fields. *Biol. Cybern.* **27**, 77–87, DOI: 10.1007/BF00337259 (1977).

25. Coombes, S., Graben, P. B. & Potthast, R. *Neural Fields* (Springer Berlin Heidelberg, Berlin, Heidelberg, 2014).

26. Spreizer, S., Aertsen, A. & Kumar, A. From space to time: Spatial inhomogeneities lead to the emergence of spatiotemporal sequences in spiking neuronal networks. *PLOS Comput. Biol.* **15**, e1007432, DOI: 10.1371/journal.pcbi.1007432 (2019).

27. Kim, S. S., Rouault, H., Druckmann, S. & Jayaraman, V. Ring attractor dynamics in the Drosophila central brain. *Science* **356**, 849–853, DOI: 10.1126/science.aal4835 (2017).

28. Zhang, K. Representation of spatial orientation by the intrinsic dynamics of the head-direction cell ensemble: a theory. *The J. Neurosci.* **16**, 2112–2126, DOI: 10.1523/JNEUROSCI.16-06-02112.1996 (1996).

29. Lehr, A. B., Kumar, A. & Tetzlaff, C. Dynamic control of neural manifolds. *BioRxiv* DOI: 10.1101/2024.07.08.602452 (2024).

30. Allen Mouse Spinal Cord Atlas. https://mousespinal.brain-map.org/.

31. Russ, D. E. *et al.* A harmonized atlas of mouse spinal cord cell types and their spatial organization. *Nat. Commun.* **12**, DOI: 10.1038/s41467-021-25125-1 (2021).

32. Kozlov, A., Huss, M., Lansner, A., Kotaleski, J. H. & Grillner, S. Simple cellular and network control principles govern complex patterns of motor behavior. *Proc. Natl. Acad. Sci.* **106**, 20027–20032, DOI: 10.1073/pnas.0906722106 (2009).

33. Bácskai, T., Rusznák, Z., Paxinos, G. & Watson, C. Musculotopic organization of the motor neurons supplying the mouse hindlimb muscles: a quantitative study using Fluoro-Gold retrograde tracing. *Brain Struct. Funct.* **219**, 303–321, DOI: 10.1007/s00429-012-0501-7 (2014).

34. Ronzano, R. *et al.* Spinal premotor interneurons controlling antagonistic muscles are spatially intermingled. *eLife* **11**, DOI: 10.7554/eLife.81976 (2022).

35. Capelli, P., Pivetta, C., Esposito, M. S. & Arber, S. Locomotor speed control circuits in the caudal brainstem. *Nature* **551**, 373–377, DOI: 10.1038/nature24064 (2017).

36. Gosgnach, S. *et al.* V1 spinal neurons regulate the speed of vertebrate locomotor outputs. *Nature* **440**, 215–219, DOI: 10.1038/nature04545 (2006).

37. Falgairolle, M. & O'Donovan, M. J. V1 interneurons regulate the pattern and frequency of locomotor-like activity in the neonatal mouse spinal cord. *PLOS Biol.* **17**, e3000447, DOI: 10.1371/journal.pbio.3000447 (2019).

38. Falgairolle, M. & O'Donovan, M. J. Optogenetic Activation of V1 Interneurons Reveals the Multimodality of Spinal Locomotor Networks in the Neonatal Mouse. *The J. Neurosci.* **41**, 8545–8561, DOI: 10.1523/JNEUROSCI.0875-21.2021 (2021).

39. Callahan, R. A. *et al.* Spinal V2b neurons reveal a role for ipsilateral inhibition in speed control. *eLife* **8**, 1–27, DOI: 10.7554/eLife.47837 (2019).

40. Talpalar, A. E. *et al.* Dual-mode operation of neuronal networks involved in left-right alternation. *Nature* **500**, 85–88, DOI: 10.1038/nature12286 (2013).

41. Kiehn, O. Decoding the organization of spinal circuits that control locomotion. *Nat. Rev. Neurosci.* **17**, 224–238, DOI: 10.1038/nrn.2016.9 (2016).

42. Brown, T. G. On the nature of the fundamental activity of the nervous centres; together with an analysis of the conditioning of rhythmic activity in progression, and a theory of the evolution of function in the nervous system. *J Physiol* **48**, 18–46, DOI: 10.1113/jphysiol.1914.sp001646 (1914).

43. Lindén, H. & Berg, R. W. Why Firing Rate Distributions Are Important for Understanding Spinal Central Pattern Generators. *Front. Hum. Neurosci.* **15**, 719388, DOI: 10.3389/fnhum.2021.719388 (2021).

44. Dale, N. Coordinated Motor Activity in Simulated Spinal Networks Emerges from Simple Biologically Plausible Rules of Connectivity. *J. Comput. Neurosci.* **14**, 55–70, DOI: 10.1023/A:1021176301776 (2003).

45. Sweeney, L. B. *et al.* Origin and Segmental Diversity of Spinal Inhibitory Interneurons. *Neuron* **97**, 341–355, DOI: 10.1016/j.neuron.2017.12.029 (2018).

46. Fetcho, J. R. & McLean, D. L. Some principles of organization of spinal neurons underlying locomotion in zebrafish and their implications. *Ann NY Acad Sci* **1198**, 94–104, DOI: 10.1111/j.1749-6632.2010.05539.x (2010).

47. Liu, Y., Hasegawa, E., Nose, A., Zwart, M. F. & Kohsaka, H. Synchronous multi-segmental activity between metachronal waves controls locomotion speed in Drosophila larvae. *eLife* **12**, DOI: 10.7554/eLife.83328 (2023).

48. Saltiel, P., d'Avella, A., Wyler-Duda, K. & Bizzi, E. Synergy temporal sequences and topography in the spinal cord: evidence for a traveling wave in frog locomotion. *Brain Struct. Funct.* **221**, 3869–3890, DOI: 10.1007/s00429-015-1133-5 (2016).

49. Ryczko, D. *et al.* Flexibility of the axial central pattern generator network for locomotion in the salamander. *J. Neurophysiol.* **113**, 1921–1940, DOI: 10.1152/jn.00894.2014 (2015).

50. Falgairolle, M. & Cazalets, J. Metachronal coupling between spinal neuronal networks during locomotor activity in newborn rat. *The J. Physiol.* **580**, 87–102, DOI: 10.1113/jphysiol.2006.115709 (2007).

51. Cazalets, J. R., Sqalli-Houssaini, Y. & Clarac, F. Activation of the central pattern generators for locomotion by serotonin and excitatory amino acids in neonatal rat. *The J. Physiol.* **455**, 187–204, DOI: 10.1113/jphysiol.1992.sp019296 (1992).

52. Bonnot, A., Whelan, P. J., Mentis, G. Z. & O'Donovan, M. J. Locomotor-like activity generated by the neonatal mouse spinal cord. *Brain Res. Rev.* **40**, 141–151, DOI: 10.1016/S0165-0173(02)00197-2 (2002).

53. Machado, T. A., Pnevmatikakis, E., Paninski, L., Jessell, T. M. & Miri, A. Primacy of Flexor Locomotor Pattern Revealed by Ancestral Reversion of Motor Neuron Identity. *Cell* **162**, 338–350, DOI: 10.1016/j.cell.2015.06.036 (2015).

54. Cazalets, J. Metachronal propagation of motoneurone burst activation in isolated spinal cord of newborn rat. *The J. Physiol.* **568**, 583–597, DOI: 10.1113/jphysiol.2005.086850 (2005).

55. Pérez, T. *et al.* An Intersegmental Neuronal Architecture for Spinal Wave Propagation under Deletions. *The J. Neurosci.* **29**, 10254–10263, DOI: 10.1523/JNEUROSCI.1737-09.2009 (2009).

56. Cuellar, C. A. *et al.* Propagation of Sinusoidal Electrical Waves along the Spinal Cord during a Fictive Motor Task. *J. Neurosci.* **29**, 798–810, DOI: 10.1523/JNEUROSCI.3408-08.2009 (2009).

57. Auyong, N., Ollivier-lanvin, K. & Lemay, M. A. Preferred locomotor phase of activity of lumbar interneurons during air-stepping in subchronic spinal cats. *J Neurophysiol* **105**, 1011–1022, DOI: 10.1152/jn.00523.2010. (2011).

58. Friedmann, D. *et al.* Mapping mesoscale axonal projections in the mouse brain using a 3D convolutional network. *Proc. Natl. Acad. Sci.* **117**, 11068–11075, DOI: 10.1073/pnas.1918465117 (2020).

59. Hennequin, G., Agnes, E. J. & Vogels, T. P. Inhibitory Plasticity: Balance, Control, and Codependence. *Annu. Rev. Neurosci.* **40**, 557–79, DOI: 10.1146/annurev-neuro-072116-031005 (2017).

60. Berg, R. W., Alaburda, A. & Hounsgaard, J. Balanced inhibition and excitation drive spike activity in spinal half-centers. *Science* **315**, DOI: 10.1126/science.1134960 (2007).

61. Petersen, P. C., Vestergaard, M., Jensen, K. H. R. & Berg, R. W. Premotor Spinal Network with Balanced Excitation and Inhibition during Motor Patterns Has High Resilience to Structural Division. *J Neurosci* **34**, 2774–2784, DOI: 10.1523/JNEUROSCI.3349-13.2014 (2014).

62. Cable, D. M. *et al.* Cell type-specific inference of differential expression in spatial transcriptomics. *Nat. Methods* **19**, 1076–1087, DOI: 10.1038/s41592-022-01575-3 (2022).